Romanian Reports in Physics **76**, 502 (2024)

INVESTIGATION OF POLYPYRROLE/TiO_2 AND POYPYRROLE/WO_3 NANOCOMPOSITES AS ANODE MODIFIER IN SALT BRIDGE MICROBIAL FUEL CELL USING MUNICIPAL WASTEWATER

ANCA DUMITRU*, AURELIA DINU, IOANA C. IURESCU, STEFAN TOADER

University of Bucharest, Faculty of Physics, PO Box MG-11, 077125, Magurele, Romania
*Coresponding author: *anca.dumitru@ unibuc.ro*

Recieved July 30, 2023

Abstract. Developing nanocomposite materials based on conducting polymers (CPs) and metal-oxide nanoparticles, which combine redox electrochemistry of CPs with intrinsic properties of nano-scale semiconducting materials, may offer improved microbial fuel cells (MFCs) performances. Polypyrrole (PPY) based nanocomposites were synthesized by chemical oxidative polymerization method and were further used as an anode modifier in salt bridge MFCs. The PPY-based nanocomposites were characterized by X-ray diffraction, Fourier-Transform Infrared (FTIR) spectroscopy, and Scanning Electron Microscopy (SEM). The maximum power density of 16.7 mW/m^2, 20.1 mW/m^2, and 22.5 mW/m^2 were obtained for MFC2-PPY, MFC3-PPY/TiO_2 and MFC4-PPY/WO_3 respectively, suggesting that modification of the anode with PPY-based nanocomposites is beneficial in the electricity generation of the MFC, and have superior performance as compared to the controller MFC1-CC (11.6 mW/m^2).

Key words: polypyrrole/TiO_2, polypyrrole/WO_3, nanocomposite, anode modification, salt bridge microbial fuel cell.

DOI: https://doi.org/10.59277/RomRepPhys.2024.76.502

1. INTRODUCTION

Water pollution, water shortages, and energy crises are one of the main issues of our society and, as a consequence, the development of new environmentally friendly solutions has become a necessity [1–4]. In this aim, microbial fuel cells (MFCs) represent a solution that can combine both green energy production and wastewater treatment in a single step through metabolic activities of microorganisms [1, 2, 5]. A typical double-chamber MFCs consists of one anaerobic chamber containing exoelectrogenic bacteria responsible for transferring electrons to the anode and an aerobic cathode chamber separated by a proton exchange membrane [2, 5]. Despite the remarkable progress achieved in the performance improvement of MFCs, the relatively low power density and low removal efficiency limits the application of MFCs at a commercial scale [1, 6].

One of the important limiting factors underlying the low efficiency of MFCs is the characteristics of the anode electrode material, which needs to provide a high surface area for bacterial growth [1, 2, 5, 6]. In order to improve the MFCs performance, various nanomaterials with different morphology (*e.g.*, nanowires, nanotubes, thin films or nanoparticles) and nanocomposites based on conducting polymers with carbon nanomaterials, metal or metal oxide nanoparticles have been considered as a strategy for anode modification [6–9]. One of the trends in the development of efficient MFCs is related to anode modification with nanocomposite materials which offer the advantages of the synergetic effect of both components. Most of the studies of conducting polymer based nanocomposite were focused on the development of nanocomposite materials based on conducting polymers (CPs) with carbon nanostructures, which combine the properties of carbon nanostructure with redox electrochemistry of CPs [10–12]. Unfortunately, limited studies have been reported the use of nanocomposites based on metal or metal-oxide nanoparticles for anode modification, even most of the review papers related to anode modification recommend it as further investigation [1, 2, 6, 7]. Among them, the modification of stainless steel mesh with an anode of polypyrrole (PPY) nanotube coated with chitosan and nickel oxide as a biocompatible anode generated a power density of 755 mW/m^2, which is 4.4 times higher than the power density of bare stainless steel anode (170 mW/m^2) [13]. Phonsa *et al.*, reported that MnO_2/PPY-coated stainless steel electrode improved the MFCs efficiency and had a maximum power density of 440 mW/m^2 and almost 100% of COD (Chemical Oxygen Demand) removal [14]. Prakash *et al.*, investigated the electrochemical performances of PPY coated MnO_2 and MnO_2-Fe_2O_3 nanocomposites as anode modifier in benthic microbial fuel cells. The results showed the PPY coated with Fe_2O_3 exhibited a higher power density (170 mW/m^2) than that of unmodified electrodes (69.19 mW/m^2) [15]. Nanostructured 30 wt% polyaniline/TiO_2 composite presented a very promising catalytic activity, showing a maximum power density of 1495 mW/ m^2 [16]. Benetton *et al.*, reported a high power density of 2317 mW/m^2 for MFCs that uses *Geobacter sulfurreducens* as sole biocatalyst and Ti/TiO_2-polyaniline (PANI) anodes [17]. A better performance of MFC with PANI composite TiO_2 nanosheets modified carbon paper electrode was attributed to the synergistic effect between vertically oriented TiO_2 nanosheets and PANI, which significantly reduced the charge transfer resistance at the anode interface [18]. Mesoporous composite PANI/m-WO_3 that combines the biocompatibility of WO_3 with the conductivity of PANI was proposed as a novel anode electrocatalyst for high performance of MFC by Wang *et al.* Their results suggested that the contribution of the improved electrochemical activity of PANI due to the interaction between PANI and m-WO_3 plays an important role in the electricity generation of the MFC [19]. Therefore, for enhancing MFC performance is essential that the nanocomposite materials used for anode modification to have a high compatibility with the host bacteria that can favor the formation of biofilm and the direct oxidation of metabolites.

In this regard, PPY, due to its excellent conductivity, stability, and biocompatibility combined with the intrinsic properties of nano-scale semiconducting materials such as TiO_2 and WO_3, has been used for the development of PPY-TiO_2 and PPY-WO_3 nanocomposites. The resulting nanocomposite materials were further used as anode modifiers in low-cost salt bridge microbial fuel cells loaded with municipal wastewater, which, to our knowledge, has not been reported in the existing literature.

2. EXPERIMENTAL DETAILS

2.1. MATERIALS

TiO_2 nanopowder (a mixture of anatase and rutile phases, with particles size < 100 nm), WO_3 nanoparticles (particle size of ~100 nm), pyrrole monomer (97% purity), ferric chloride hexahydrate, para-toluene sulfonate (PTS), ethanol and acetone were purchased from Sigma-Aldrich and were used as received. Commercially multi-wall carbon nanotubes (MWCNTs) with diameters between 20 and 40 nm and purity > 97% were purchased from Shenzhen Nanotech Co. Ltd.

2.2. NANOCOMPOSITE SYNTHESIS

PPY and PPY-based nanocomposites were synthesized by chemical oxidative polymerization method in 20% aqueous methanol solution using $FeCl_3$ as oxidant and PTS as the dopant. 0.1 M of TiO_2 nanoparticles or WO_3 nanoparticles were dispersed in 20% aqueous methanol solution and stirred for 30 min. 0.1 M pyrrole monomers and 0.2 M PTS were added to the prepared solution and the mixture was vigorously stirred for 30 minutes. Then 0.2 M ferric chloride hexahydrate dissolved in 20% aqueous methanol solution was added to the above solution, drop by drop in 15 minutes duration, under stirring conditions. After continuous stirring for 6 h at room temperature, the powder was collected and washed copiously several times with distilled water and ethanol, in order to remove the residual oxidant. At the end, the powder was washed with acetone and dried at 60°C for several hours. The samples were indexed as PPY/TiO_2 and PPY/WO_3, respectively. Polypyrrole (PPY) was synthesized in the same way in the absence of oxide nanoparticles.

2.3. MATERIAL CHARACTERIZATIONS

Fourier Transform Infrared (FTIR) Spectroscopy analysis of the PPY and PPY-based nanocomposites was performed using Varian 3100 Excalibur spectrophotometer (Varian, Palo Alto, CA, USA), in the spectral range of 600–4000 cm^{-1}, with a resolution of 4 cm^{-1}, by attenuated total reflection (ATR) using a Pike MIRacle

(Ge crystal) accessory. The crystalline features of PPY and PPY-based nanocomposites were characterized by X-ray diffraction (XRD) using a Bruker D8 Discover diffractometer using CuKα radiation (λ = 1.5406 Å), in symmetric geometry. The morphological characteristics of PPY and PPY-based nanocomposites were analyzed using Scanning Electron Microscopy (SEM) (Tescan MAIA-3 field-emission electron microscope, TESCAN, Brno, Czech Republic).

2.4. MICROBIAL FUEL CELL SETUP AND OPERATION

A double-chamber salt bridge MFC with an H-type configuration was used to test the performance of the anode modified with PPY-based nanocomposites. The salt bridge MFCs were made by joining the anode and cathode chambers with a plastic tube containing a salt bridge, which was used as a more economical replacement for the proton exchange membrane (Nafion). For each MFC configuration, two equal volume plastic bottles (275 ml) with a side opening connected by a horizontal salt bridge (diameter = 1.5 cm, length = 6 cm) sealed to the containers were used. To avoid the leakage, epoxy glue was applied. The salt-bridge contained a mixture of 1M potassium chloride with 10% Agar (w/v). Anodes were made of non-wet proofed carbon cloth (CC) modified using an airbrush, with a suspension of PPY-based nanocomposites (1 mg/mL) in ethanol aqueous solution (1:1 v/v) containing 0.5% Nafion. For cathodes, MWCNTs ink containing the chemical binder (5% Nafion solution) was sprayed over CC. The configuration of salt bridge MFCs evaluated in our work are summarized in Table 1.

Table 1

Configuration of salt bridge MFCs

MFC index	Anode	Cathode
MFC1	CC	MWCNTs
MFC2	PPY	MWCNTs
MFC3	PPY/TiO_2	MWCNTs
MFC4	PPY/WO_3	MWCNTs

Anode and cathode were connected to the external circuits, containing a 1 kohm resistor, using copper wires. The exposed copper metal surface at the joints was tightly sealed with a non conductive epoxy resin. The anolyte consisted of municipal wastewater (Water Distribution and Sewerage Company, Magurele SRL, Ilfov Romania) supplemented with 1 g/L of acetate and phosphate buffer (0.05 M, pH 7.0 ± 0.01) was used as the catholyte. The anode chamber was hermetically sealed, while the cathode chamber was purged with bubbling air. All experiments were carried out at ambient temperature. Cell voltages across the external resistor were recorded using a Pico Data Logger ADC-24 (Pico Technology, Cambridgeshire, UK). The performance of all MFCs was evaluated through the polarization and power

density curves. The polarization and power density curves were obtained by varying the external resistor from 1 Mohm to 40 ohm. The open cell potential (OCP) was measured after 120 min. To ensure that a stable power output had been achieved, for each electrical resistance, MFCs ran for at least 10 min. Current intensity (I) was calculated as $I = V$ (cell voltage)/R (external electrical resistance), and the electrical power (P) was calculated as $P = I \cdot V$. Both current density and power density were calculated based on the surface area of the anode. The slope of the polarization curve was used to determine the internal electrical resistance of MFCs.

3. RESULTS AND DISCUSSIONS

3.1. CHARACTERIZATION PPY-BASED NANOCOMPOSITES

To confirm the synthesis of PPY-based nanocomposites, FTIR spectroscopy of the synthesized materials was performed. The infrared spectra of PPY and PPY-based nanocomposites in the spectral region from 1800 cm^{-1} to 600 cm^{-1} are shown in Fig. 1.

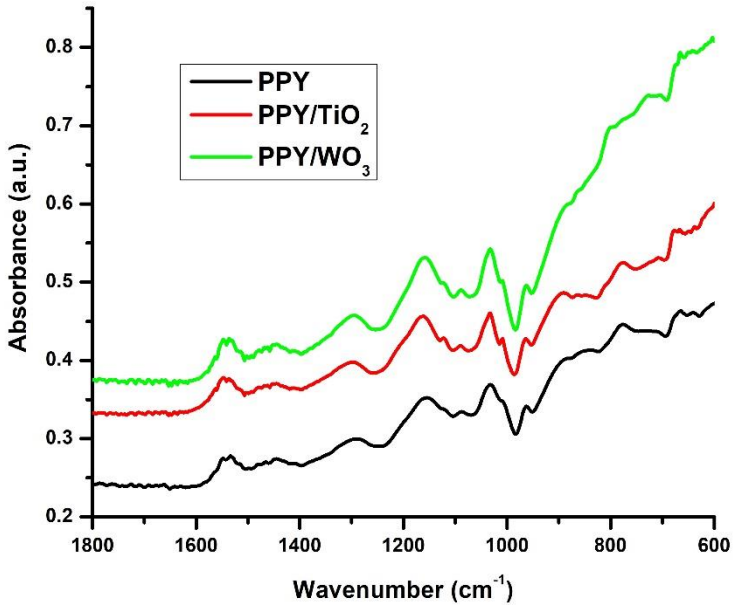

Fig. 1 – FTIR spectra of PPY, PPY/TiO_2 and PPY/WO_3 nanocomposites.

The FTIR spectrum of PPY shows the peaks at 1542 cm^{-1} and 1452 cm^{-1} attributed to the characteristic absorption of C = C stretching vibrations in pyrrole ring [20, 21]. The absorption band between 1250–1390 cm^{-1} with a maximum at 1296 cm^{-1} is attributed to C–H or C–N stretching vibrations in the pyrrole ring, while the band at 1160 cm^{-1} to C-H stretching of the pyrrole ring [20, 22]. The absorption

peak at 1117 cm^{-1} is attributed to the breathing vibrations of the pyrrole ring [22] and the absorption between 1100 and 980 cm^{-1} corresponds to C-H in-plane deformation and out-of-plane deformation vibrations [20, 22]. The peak at 890 cm^{-1} corresponds to C-C out-of-plane ring deformation vibrations, while the one located at 778 cm^{-1} may be attributed to C–H out-of-plane ring deformation or C-N vibrations. The maximum located at 674 cm^{-1} is attributed to C-C out-of-plane ring deformation or C–H rocking [20–22]. The spectra of PPY/TiO_2 and PPY/WO_3 showed the presence of the characteristic PPY bands (1800–600 cm^{-1}) with a slight displacement or an attenuation of the intensity as a result of the interaction between PPY and TiO_2 or WO_3 nanoparticles, respectively.

Figure 2 shows the X-ray diffraction (XRD) of commercially TiO_2 nanoparticles, synthesized PPY and PPY-TiO_2 nanocomposites. X-ray diffraction pattern of PPY shows few broad diffraction peaks between 10° and 30°, which are characteristic of the amorphous phase of PPY and are attributed to the scattering from PPY chains at the interplanar spacing [11].

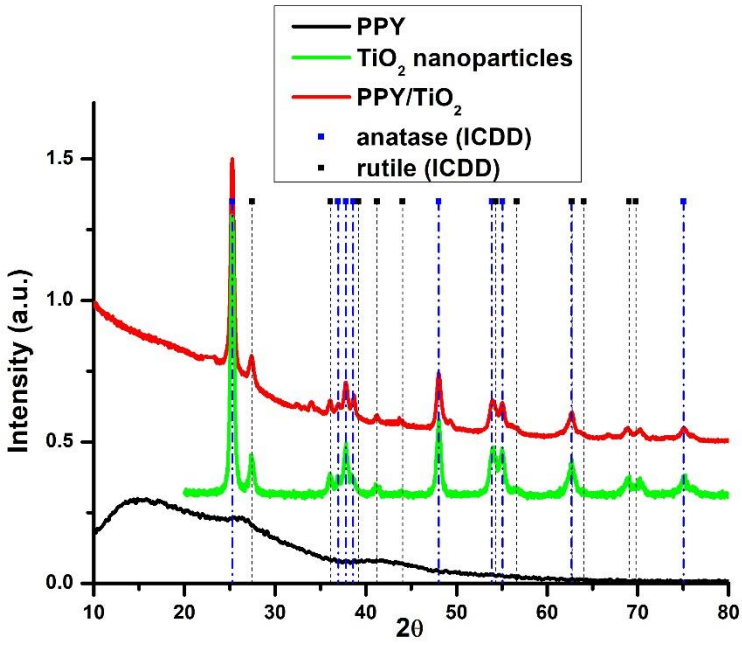

Fig. 2 – X-ray diffraction of PPY, TiO_2 nanoparticles and PPY/TiO_2 nanocomposite.

As expected, the XRD pattern of commercial TiO_2 nanoparticles exhibits main diffraction peaks indexed as (101), (103), (004), (112), (200), (105), (211), (204), and (215), reflections of anatase crystalline phase, corresponding to those shown in the International Centre for Diffraction Data (ICDD) database card No. 00-021-1272. The main diffraction peaks indexed as (110), (101), (200), (111), (210), (211),

(220), (002), (310), (301), and (112) are assigned to rutile crystalline phase, corresponding to those shown in the ICDD card No. 00-021-1276. X-ray diffraction patterns of PPY-CNT have a similar shape to that of TiO_2 nanoparticles, which proves the presence of the TiO_2 phase in the PPY-based nanocomposites.

Figure 3 presents the XRD results of PPY, WO_3 nanoparticles and PPY/WO_3 nanocomposites. The diffraction patterns of the WO_3 nanoparticles correspond to the peaks of monoclinic WO_3 (ICDD 01-083-0950). In the case of PPY/nanocomposites, beside the characteristic reflection of WO_3, a broad diffraction peak between 10° and 20° appears due to the presence of the amorphous phase of PPY in nanocomposite materials. The patterns of both nanocomposites indicate that PPY deposited on the surface of TiO_2 or WO_3 nanoparticles has no effect on the crystallization characteristics of TiO_2 or WO_3, respectively. Thus, FTIR and XRD results, as complementary measurements, confirm the synthesis of PPY-based nanocomposites.

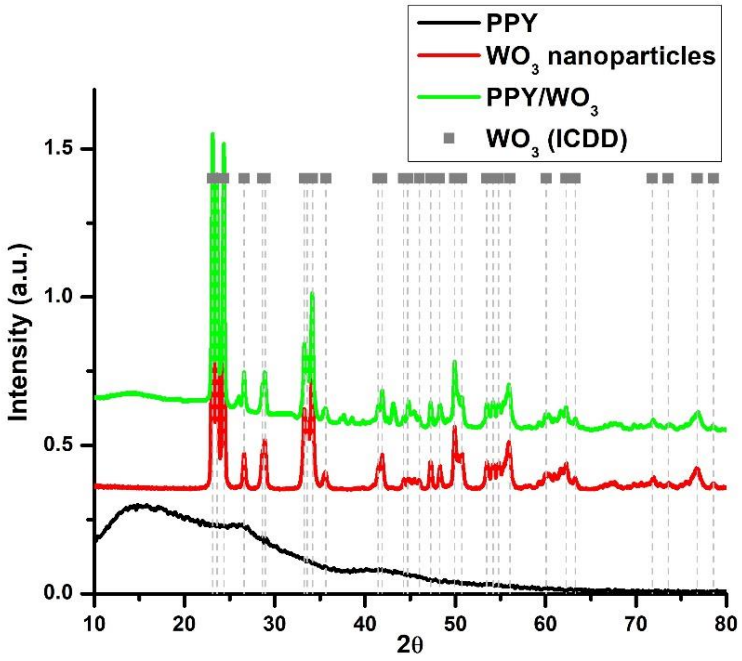

Fig. 3 – X-ray diffraction of PPY, WO_3 nanoparticles and PPY/WO_3 nanocomposite.

The morphological features of polypyrrole, metal oxide nanoparticles, and PPY-based nanocomposites are presented in Fig. 4. SEM images of PPY (Fig. 4a and 4b) have revealed the growth is mostly in a globular form, and because the individual granules adhered to each other, aggregations appeared. In the case of PPY-based nanocomposites, the incorporation of TiO_2 and WO_3 nanoparticles did not affect the particles' morphology but is more difficult to be distinguished, showing a much closed-packed structure.

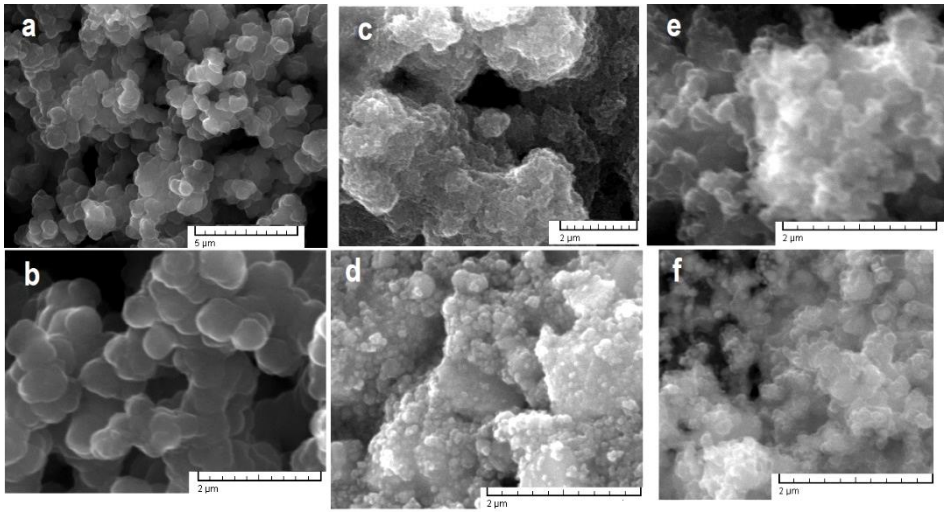

Fig. 4 – SEM image of a) and b) PPY; c) TiO_2 nanoparticles; d) WO_3 nanoparticles; e) PPY/TiO_2 nanocomposites, and f) PPY/WO_3 nanocomposites.

3.3. MICROBIAL FUEL CELL PERFORMANCE

Figures 5 and 6 show the polarization curves obtained for MFC1, MFC2, MFC3 and MFC4, after the first and second polarization. The OCP, maximum power density and internal electrical resistance of the cell were summarized in Table 2. The first polarization was carried out in the first fed-batch cycle after the MFCs reached the steady state and the second polarization was done on the second fed-batch cycle, after the anolyte replacement, once the MFCs reached steady state. The improvement of overall performance of MFCs suggests a better enrichment of the anode biofilm in the second fed-batch cycle. In the first fed-batch cycle, a stable voltage was detected after 12 days of continuous operation. OCPs obtained for all systems were almost similar, with values of 405 mV and 455 mV in the first fed-batch cycle and between 475 mV and 555 mV for the second fed-batch cycle (Table 2). Based on the acquired results in both fed-batch cycles, MFC4 reactor with the anode modified with PPY/WO_3 nanocomposites, had generated the highest power density of 22.5 mW/m^2 and the lowest internal electrical resistance of 0.5 kΩ, as calculated from the polarization graph. Comparing the maximum power density of the reactors, including the control (MFC1), which reached maxima at 11.6 mW/m^2, 16.7 mW/m^2, 20.1 mW/m^2, and 22.5 mW/m^2 for MFC1-CC, MFC2-PPY, MFC3-PPY/TiO_2, and MFC4-PPY/WO_3 respectively, has indicated that modification of the anode with PPY-based nanocomposites is beneficial in the electricity generation of the MFCs, as compared to the controller (MFC1-CC). Furthermore, the better performance of anode modification with PPY/WO_3 may be correlated with the synergetic effect of both WO_3 nanoparticles that provides the nanocomposite with a good biocompatibility,

and the polypyrrole, which contributes to the electrical conductivity of the nanocomposite.

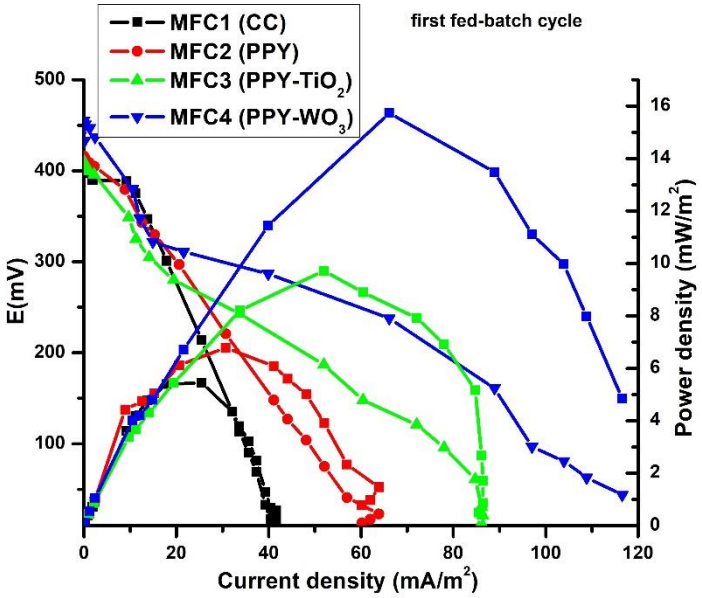

Fig. 5 – Polarization and power density curves of MFC1, MFC2, MFC3 and MFC4.

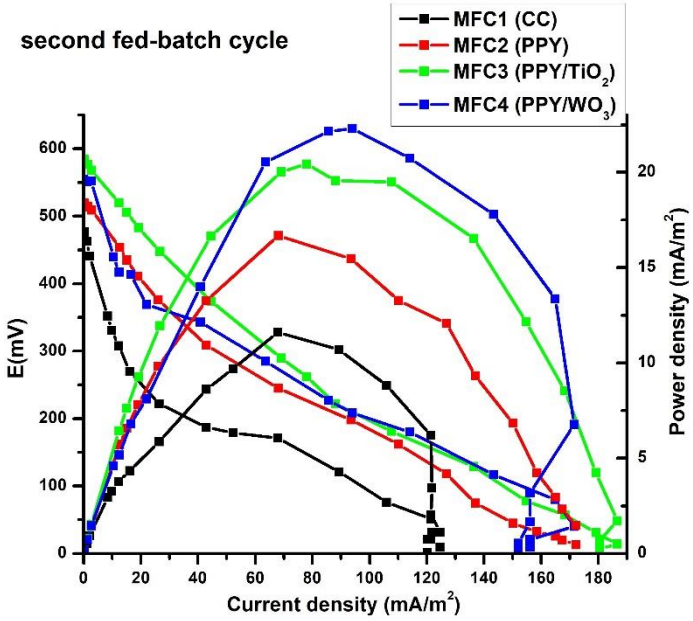

Fig. 6 – Polarization and power density curves of MFC1, MFC2, MFC3 and MFC4.

Table 2

The OCP, power density, and internal resistance of MFC1, MFC2, MFC3 and MFC4 for the first and the second fed-batch cycle

		First fed-batch cycle			Second fed-batch cycle		
Reactor	**Anode Materials**	**OCP (mV)**	**Power density (mW/m^2)**	**Internal resistance (kΩ)**	**OCP (mV)**	**Power density (mW/m^2)**	**Internal resistance (kΩ)**
MFC1	CC	405	5.4	2.7	475	11.6	2.5
MFC2	PPY	416	6.8	1.9	520	16.7	1.2
MFC3	PPY/TiO_2	410	9.7	0.9	585	20.1	0.8
MFC4	PPY/WO_3	455	15.7	0.7	555	22.3	0.5

4. CONCLUSIONS

PPY/TiO_2 and PPY/WO_3 nanocomposites have been used as anode modifier in salt bridge MFCs loaded with municipal wastewater, due to the excellent properties of PPY, such as its good conductivity, high stability, and broad biocompatibility, combined with the intrinsic properties of semiconducting TiO_2 and WO_3 nanoparticles. PPY/TiO_2 and PPY/WO_3 nanocomposites were synthesized by the chemical oxidation method. The synthesis of nanocomposites has been confirmed by the FTIR and XRD analysis. In our study, the best performance of the salt bridge MFC was obtained in the case of anode modified with PPY/WO_3 nanocomposites, which generated a maximum power density of 22.5 mW/m^2 and an internal electrical resistance of 0.5 kΩ. The obtained results showed that the anode modification with PPY-based nanocomposites is an effective method for anode modification, which can further improve the electricity generation and performance of MFCs.

Acknowledgments. This work was supported by the Romanian National Authority for Scientific Research and Innovation, CCCDI – UEFISCDI, PN-III-P4-ID-PCE-2020-0956.

REFERENCES

1. A. A. Yaqoob, M. N. M. Ibrahim, M. Rafatullah, Y. S. Chua, A. Ahmad and K. Umar, Materials **13**, 2078 (2020).
2. Y. Hindatu, M.S.M. Annuar, A.M. Gumel, Renew. Sust. Energ. Rev. **73**, 236–248 (2017).
3. M.-E. Barbinta-Patrascu, C. Nichita, S.Antohe, Rom. Rep. Phys. **75**, 604 (2023).
4. S.I. Bognar, T.B. Ivetic, B. M. Bajac, R.R. Raonic, T. Bojanic, D.S. Merkulov, Rom. J. Phys. **67**, 609 (2022).
5. Y.-J. Jiang, S. Hui, L.-P. Jiang, J.-J. Zhu, Chem. Eur. J., **29**, e202202002 (1 of 18) (2023).
6. A. Dumitru and K. Scott, *Microbial Electrochemical and Fuel Cells. Fundamentals and Applications*, Woodhead Publishing, pp. 117–152, 2015.
7. R. Kaur, A. Marwaha, V. A. Chhabra, K.-H. Kim, S.K. Tripathi, Renew. Sust. Energ. Rev. **119**, 109551 (2020).
8. S. Iftimie and A. Dumitru, Appl. Surf. Sci. **492**, 661–668 (2019).

9. I. Lascu, C. Locovei, C. Bradu, C. Gheorghiu, A. M. Tanase, A. Dumitru, Int. J. Mol. Sci. **23**, 11230 (2022).
10. J. Hou, Z. Liu, P. Zhang, J. Power Sources **224** 139–144 (2013).
11. A. Dumitru, S. Vulpe, A. Radu, S. Antohe, Rom. J. Physics **63**, 605 (2018).
12. Z. Gao, W. Yang, J. Wang, B. Wang, Z. Li, Q. Liu, M. Zhang, L. Liu, Energy Fuels **27**, 568−575 (2013).
13. Geetanjali, S. K. Dhillon, P. P. Kundu, J. Power Sources **539**, 231595 (2022).
14. S. Phonsa, P. Sreearunothai, S. Charojrochkul, K. Sombatmankhong, Solid State Ionics **316**, 125–134 (2018).
15. O. Prakash, A. Mungray, S. Chongdar, S. K. Kailasa, A. K. Mungray, J. Environ. Chem. Eng. **8**, 102757 (2020).
16. Y. Qiao, S.-J. Bao, C. Ming Li, X.-Q. Cui, Z.-S. Lu, J. Guo, ACS Nano **2**, 113–119, (2008).
17. X. D. Benetton, S.G. Navarro-Ávila, C. Carrera-Figueiras, J. New Mater. Electrochem. Syst. **13**, 1–6 (2010).
18. T. Yina, H. Zhanga, G. Yang, L. Wang, Synthetic Metals **252**, 8–14 (2019).
19. Y. Wang, B. Li, L. Zeng, D. Cui, X. Xiang, W. Li, Biosens. Bioelectron. **41**, 582–588 (2013).
20. Y. Wang, R. Song, L Li, R. Fu, Z. Liu, B. Li, Appl. Sci. **12**, 58 (2022).
21. H. K. Chitte, N. V. Bhat, V. E. Walunj, G. N. Shinde, J. Sens. Technol. **1**, 47–56 (2011).
22. M. Omastova, M. Trchova, J. Kovarova, J. Stejskal, Synth. Met. **138**, 447–455 (2003).